Comparison of Different Inflow Models for Intermeshing Rotors

Tobias Ehlert, DLR Institute of Flight Systems, 38108 Braunschweig
Feyyaz Guner†, DLR Institute of Flight Systems, 38108 Braunschweig
Andreas E. Voigt, DLR Institute of Flight Systems, 38108 Braunschweig

New inflow models have been introduced in the literature for multirotor systems with the goal to include interaction effects between the rotor. While these models have been validated for some rotor configurations, a validation for intermeshing rotor configurations has yet to be presented. This paper gives an overview over some of the existing inflow models applicable to intermeshing rotors. Flight test data is used to compare the hover trim state calculated using different inflow models: The Pitt-Peters model, the Combined Momentum Theory Simple Vortex Theory (CMTSVT) model and a simple inflow coupling introduced in a paper from Padthe et al. The comparison of flight test and simulation prediction shows that for intermeshing rotors, interaction effects must be included in the inflow model to obtain accurate rotor power and collective angle.

1. NOTATION

Symbols

A	rotor disc area, m²
C_T	aerodynamic thrust coefficient, nD
C_M, C_L	aerodynamic pitch and roll moment coefficients, nD
C_P	rotor power coefficient, nD
$\boldsymbol{F}$	rotor load vector, nD
k	interaction coefficient, nD
$\boldsymbol{L}$	inflow static gain matrix, nD
$\boldsymbol{M}$	apparent mass matrix, nD
P	rotor power, W
R	rotor radius, m
$\boldsymbol{R_\gamma}$	load relation matrix, nD
r	radial blade coordinate, nD
V	forward flight velocity, $\frac{m}{s}$; mass flow parameter, nD
V_T	total flow through rotor disc, nD
α^*	wake skew angle proxy, rad
λ	inflow velocity, nD
λ_0	uniform inflow component, nD
λ_c	longitudinal inflow component, nD
λ_s	lateral inflow component, nD
ρ	air density, kg/m³
χ	wake skew angle, rad
ψ	azimuth angle, rad
Ω	main rotor speed of rotation, rad/s

† Currently works at Joby Aviation.

2. INTRODUCTION

The modeling of rotor-rotor interactions has gained increasing prominence in rotorcraft simulation, particularly with the recent advancements in both computationally demanding grid-based methods and reduced-order wake-based models. These models depict the induced flow through the rotor disc, hence they are designated as inflow models.

For real-time flight simulations, high fidelity models based on Computational Fluid Dynamics (CFD) or Vortex Particle Methods (VPM) are often not feasible. Wake models based on potential flow theory can provide the desired balance of simulation fidelity and processor run time. Most recent literature uses combinations of momentum theory and a vortex model [1] [2] [3] One of those models is the Combined Momentum Theory Simple Vortex Theory (CMTSVT) model developed by Guner in [1]. The model has however yet to be validated for Flettner configurations, i.e. a rotor configuration of intermeshing rotors.

The DLR Institute of Flight Systems operates a SwissDrones 50 rotorcraft, called superARTIS, for flight guidance research, as well as investigating the specific flight mechanics of intermeshing rotors (Figure 1). To support ongoing research activities, the rotorcraft is modified with an experimental measurement system capable of recording both the flight mechanical state variables and in-flight rotor mechanical variables.

Further, the institute has developed the Versatile Aeromechanical Simulation Tool (VAST), a utility designed for simulating rotorcraft flight mechanics. Its design provides a flexible interface for integrating relevant physical models, simplifying the incorporation of new inflow models.

This paper seeks to validate the effect of inflow models on intermeshing rotor power calculations. A simple empirical model is also presented as a reference, illustrating how a simple correction can significantly improve performance calculations.

This paper is structured as follows: After introducing the theoretical foundations of the discussed inflow models, the superARTIS rotorcraft is presented. A simulation study is performed, with the aim of determining performance characteristics at hover. Finally, the effects of the inflow models on performance calculation are examined.

3. Inflow Models

The literature provides a wide variance of inflow models for helicopters. In the following, a short overview is provided. We then focus on a selection of those contributions, which are relevant for real-time flight simulation.

By the time Hermann Glauert published his fundamental works on rotorcraft flight mechanics, he already emphasized on the importance of the rotor inflow [4] [5]. He first postulated a uniform inflow which was later extended by a longitudinal component for forward flight.

The advantage of hingeless rotors lead to the development of a new inflow model by Peters and Ormiston: Because their relatively large hub moments, the inflow has to be modelled using a mean, longitudinal and lateral component [6] [7]. This model is based on momentum theory and only valid for steady states. Pitt and Peters later developed a dynamic model that is based on potential theory [8]. This model in its formulation from 1988 is typically called the “Pitt-Peters Model”.

Another line of models is based on describing the rotor wake, how it develops over time and which velocity field it induces on the rotor disc. Prescribed wake models often have a simpler model structure, which makes them faster to calculate but less accurate. Free vortex wake models have a much more complex model structure, which makes them computationally expensive, but well suited for computing dynamic maneuvers within geometrically complex environment with relatively high accuracy [9] [10].

3.1. Pitt and Peters

The inflow model from Pitt and Peters is a state-space model with a state vector of the form

(1) $$\boldsymbol{\lambda} = (\lambda_0, \lambda_s, \lambda_c)^T.$$

This is a form of varying the inflow over blade azimuth ψ and radius r:

(2) $$\lambda(r,\psi) = \lambda_0 + \frac{r}{R}\lambda_s \sin\psi + \frac{r}{R}\lambda_c \cos\psi$$

Equation (2) only includes inflow harmonics of the first order, so it can be seen as a filter for higher harmonics, since those are neglected.

The governing equation

(3) $$(\boldsymbol{L}\boldsymbol{V}^{-1})^{-1}\boldsymbol{\lambda} + \boldsymbol{M}\overset{*}{\boldsymbol{\lambda}} = \boldsymbol{F}$$

uses the normalized derivation of the inflow state $\overset{*}{\boldsymbol{\lambda}} = {}^{\partial\boldsymbol{\lambda}}/_{\partial\psi} = {}^{\dot{\boldsymbol{\lambda}}}/_{\Omega\mathrm{R}}$.

In equation (3), $\boldsymbol{F}$ denotes the load vector.

(4) $$\boldsymbol{F} = (C_T, -C_L, -C_M)^T.$$

The aerodynamic loads are normalized as $C_T = \frac{T}{\rho A(\Omega R)^2}$, $C_L = \frac{M_L}{\rho AR(\Omega R)^2}$ and $C_M = \frac{M_M}{\rho AR(\Omega R)^2}$.

$\boldsymbol{M}$ is also known as the apparent mass matrix of the Pitt-Peters equation and given as

(5) $$\boldsymbol{M} = \frac{1}{\pi}\begin{bmatrix} {}^{128}/_{75} & 0 & 0 \\ 0 & {}^{16}/_{45} & 0 \\ 0 & 0 & {}^{16}/_{45} \end{bmatrix}$$

The $\boldsymbol{L}$-matrix relates the given steady-state load vector $\boldsymbol{F}$ to an inflow vector $\boldsymbol{\lambda}$, see eq.3.

(6) $$\boldsymbol{L} = \begin{bmatrix} {}^{1}/_{2} & 0 & -\frac{15\pi}{64}\sqrt{\frac{1-\sin\alpha^*}{1+\sin\alpha^*}} \\ 0 & \frac{4}{1+\sin\alpha^*} & 0 \\ \frac{15\pi}{64}\sqrt{\frac{1-\sin\alpha^*}{1+\sin\alpha^*}} & 0 & \frac{4\sin\alpha^*}{1+\sin\alpha^*} \end{bmatrix}$$

The induced inflow is not only dependent on the rotor load but also on the freestream velocity. The freestream is factored via the matrix $\boldsymbol{V}$.

$$(7) \qquad \boldsymbol{V} = \begin{bmatrix} V_T & 0 & 0 \\ 0 & V & 0 \\ 0 & 0 & V \end{bmatrix},$$

Where V is calculated with the following three equations

$$(8) \qquad \alpha^* = \tan^{-1} \frac{|\lambda + \lambda_f|}{\mu_r},$$

$$(9) \qquad V_T = \sqrt{\mu_r^2 + (\lambda + \lambda_f)^2}$$

and

$$(10) \qquad V = \frac{\mu^2 + (2\lambda_0 - \mu_3)(\lambda_0 - \mu_3)}{V_T}.$$

Since V depends on the induced velocity itself, the equation can only be solved iteratively.

Note that while the inversion of $\boldsymbol{V}$ is trivial, the inversion of $\boldsymbol{LV}^{-1}$ needs to be carried out for example by levering the LU-method.

Nondimensional induced velocity at blade elements is then calculated by

$$(11) \qquad \lambda(r,\ \psi) = \lambda_0 + \lambda_s \frac{r}{R} \sin\psi\ + \lambda_c \frac{r}{R} \cos\psi.$$

3.2. Padthe et al. inflow model

Padthe et al. used the following approach to correct the inflow model for a coaxial rotor [11]. For simplicity, we call this simple model correction technique *the model by Padthe et al*. It can also be seen as a reduction of CMTSVT to uniform inflow coupling.

Given a double-rotor configuration, we denote the inflow of the rotors $\boldsymbol{\lambda}^i = \boldsymbol{\lambda}^{ii} + \boldsymbol{\lambda}^{ij}$ with $\boldsymbol{\lambda}^i$ with $i \in \{1,2\}$.

Each rotor is assigned a self-induced inflow λ^{ii} and a part that is induced by the second rotor λ^{ij}. The interference part is calculated by

$$(12) \qquad \boldsymbol{\lambda}^{ij} = \boldsymbol{K}^{ij} \cdot \boldsymbol{\lambda}^{jj}.$$

Padthe et al. chose to only considered the mean inflow in their interference model, leading to

$$(13) \qquad \boldsymbol{K}^{ij} = \begin{bmatrix} k_{00}^{ij} & 0 & 0 \\ 0 & 0 & 0 \\ 0 & 0 & 0 \end{bmatrix}.$$

The effect of interfering inflow on flight performance is generally reduced at higher velocities as the wake vortices are transported off the rotor disc more quickly. This is considered by phasing out K_{00}^{ij} over increasing airspeed V:

$$(14) \qquad k_{00}^{ij} = \begin{cases} k^{ij} & V \leq V_{\text{reduce}} \\ k^{ij} \cdot \frac{V_{\text{cutoff}} + V_{\text{reduce}} - V}{V_{\text{cutoff}}} & \text{for } V_{\text{reduce}} < V < V_{\text{cutoff}} \\ 0 & V_{\text{cutoff}} < V \end{cases}$$

k_{00}^{ij} is plotted as a function of airspeed in Figure 1.

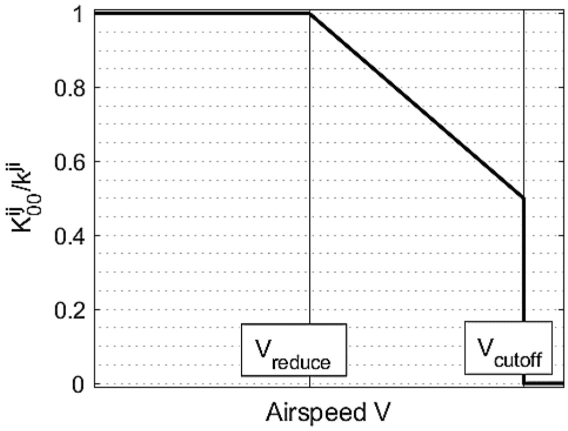

Figure 1: Interference inflow is phased out over increasing airspeed.

Therefore, the induced velocity at blade elements becomes

$$(15) \qquad \lambda^i(r,\ \psi) = (\lambda_0^{ii} + \lambda_o^{ij}) + \lambda_s^{ii} \frac{r}{R} \sin\psi\ + \lambda_c^{ii} \frac{r}{R} \cos\psi.$$

This inflow velocity is normalized by the term ΩR.

3.3. Combined Momentum Theory and Simple Vortex Theory Inflow Model

The Combined Momentum Theory and Simple Vortex Theory (CMTSVT) model has been developed by Guner in [1]. Validation studies have been performed in [1] [2] [12]. The model is given in its state-space form for dual rotors.

We describe the inflow as sum of self-induced inflow $\boldsymbol{\lambda}^{ii}$ (calculated by Pitt Peters model) and interference inflow $\boldsymbol{\lambda}^{ij}$. Other than the model by Padthe et al., CMTSVT describes interference inflow in the three Pitt-Peters states so that induced inflow at the blade elements becomes

$$(16) \qquad v^i(r,\ \psi) = (\lambda_0^{ii} + \lambda_o^{ij}) + (\lambda_s^{ii} + \lambda_s^{ij}) \frac{r}{R} \sin\psi\ + (\lambda_c^{ii} + \lambda_c^{ij}) \frac{r}{R} \cos\psi.$$

The self-induced inflow λ_0^{ii} is altered by the interference inflow because its calculation depends on the total flow passing the rotor disc:

(17) $$\lambda_0^{ii} = \frac{C_T^i}{2V_T^i},$$

where

(18) $$V_T^i = \sqrt{(\mu^i)^2 + \left(\lambda_f + \lambda_0^i\right)^2},$$

(19) $$\lambda_0^i = \lambda_0^{ii} + \lambda_0^{ij}.$$

This leads to an iterative loop in which self-induced inflow of both rotors are calculated until they converge.

The interference inflow $\boldsymbol{\lambda^{ij}}$ is calculated by

(20) $$\boldsymbol{\lambda^{ij} = L^{ij}\lambda^{jj}}.$$

Where $\boldsymbol{L^{ij}}$ is defined as

(21) $$\boldsymbol{L^{ij} = G^{ij}R_\gamma^{ij}L^{jj}}.$$

The load relation matrix $\boldsymbol{R_\gamma^{ij}}$ is needed to convert the interference calculation, which is based on vortex strengths, into the load-based system of the differential inflow equation. Result of the vortex model of CMTSVT is represented by $\boldsymbol{G^{ij}}$.

(22) $$\boldsymbol{R_\gamma^{ij}} = \frac{1}{V_T^i}\begin{pmatrix} 1 & 0 & 0 \\ 0 & 3 & 0 \\ 0 & 0 & 3 \end{pmatrix}$$

(23) $$\boldsymbol{G^{ij}} = \begin{pmatrix} g_{00}^{ij} & g_{01c}^{ij} & g_{01s}^{ij} \\ g_{1c0}^{ij} & g_{1c1c}^{ij} & g_{1c1s}^{ij} \\ g_{1s0}^{ij} & g_{1s1c}^{ij} & g_{1s1s}^{ij} \end{pmatrix}$$

Calculation of the elements of $\boldsymbol{G}$-matrix is based on the skew angle χ and the rotor coordinates (x, y, z). Since the elements are calculated using a double integral, it can be tabulated for different wake skew angles.

(24) $$R_c^{ij} = \sqrt{1 + (x^{ij})^2 + (y^{ij})^2 + (z^{ij})^2 - 2(x^{ij}\cos\psi + y^{ij}\sin\psi)}$$

(25) $$K^{ij} = \frac{1-(x^{ij}\cos\psi + y^{ij}\sin\psi) + R_C^{ij}\sin\psi\cos\psi}{\left[R_C^{ij} + (\cos\psi - x^{ij})\sin\chi + z^{ij}\cos\chi\right]R_C^{ij}}$$

(26) $$g_{00}^{ij} = -\frac{1}{4\pi^2}\int_0^{2\pi}\int_0^1\left[\int_0^{2\pi} K^{ij} d\psi\right]\bar{r}d\bar{r}d\bar{\psi}$$

(27) $$g_{01c}^{ij} = -\frac{1}{4\pi^2}\int_0^{2\pi}\int_0^1\left[\int_0^{2\pi} K^{ij}\cos\psi\, d\psi\right]\bar{r}d\bar{r}d\bar{\psi}$$

(28) $$g_{01s}^{ij} = -\frac{1}{4\pi^2}\int_0^{2\pi}\int_0^1\left[\int_0^{2\pi} K^{ij}\sin\psi\, d\psi\right]\bar{r}d\bar{r}d\bar{\psi}$$

(29) $$g_{1c0}^{ij} = -\frac{1}{\pi^2}\int_0^{2\pi}\int_0^1\left[\int_0^{2\pi} K^{ij} d\psi\right]\bar{r}^2\cos\bar{\psi}\, d\bar{r}d\bar{\psi}$$

(30) $$g_{1c1c}^{ij} = -\frac{1}{\pi^2}\int_0^{2\pi}\int_0^1\left[\int_0^{2\pi} K^{ij}\cos\psi\, d\psi\right]\bar{r}^2 d\bar{r}d\bar{\psi}$$

(31) $$g_{1c1s}^{ij} = -\frac{1}{\pi^2}\int_0^{2\pi}\int_0^1\left[\int_0^{2\pi} K^{ij}\sin\psi\, d\psi\right]\bar{r}^2\cos\bar{\psi}\, d\bar{r}d\bar{\psi}$$

(32) $$g_{1s0}^{ij} = -\frac{1}{\pi^2}\int_0^{2\pi}\int_0^1\left[\int_0^{2\pi} K^{ij} d\psi\right]\bar{r}^2\sin\bar{\psi}\, d\bar{r}d\bar{\psi}$$

(33) $$g_{1s1c}^{ij} = -\frac{1}{\pi^2}\int_0^{2\pi}\int_0^1\left[\int_0^{2\pi} K^{ij}\cos\psi\, d\psi\right]\bar{r}^2\sin\bar{\psi}\, d\bar{r}d\bar{\psi}$$

(34) $$g_{1s1s}^{ij} = -\frac{1}{\pi^2}\int_0^{2\pi}\int_0^1\left[\int_0^{2\pi} K^{ij}\sin\psi\, d\psi\right]\bar{r}^2\sin\bar{\psi}\, d\bar{r}d\bar{\psi}$$

$\boldsymbol{L^{jj}}$ differs from the L-Matrix of the Pitt-Peters model and is given as:

(35) $$\boldsymbol{L^{jj}} = \begin{pmatrix} \frac{0.5}{V_T^j} & 0 & 0 \\ 0 & \frac{4}{V^i(1+\cos\chi^j)} & 0 \\ \frac{15}{64V_T^j}\tan\frac{\chi}{2} & 0 & \frac{4\cos\chi}{V^i(1+\cos\chi^j)} \end{pmatrix}$$

4. Experimental Setup

To validate CMTSVT model, flight experiments have been performed. These featured the unmanned helicopter "Dragon 50" (SwissDrones, see Figure 2).

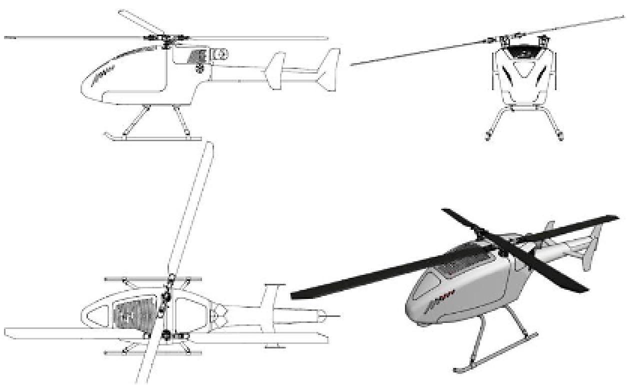

Figure 2: Helicopter side and top views and isometric view [13].

The Dragon 50 is equipped with an intermeshing rotor consisting of two hingeless two-blade rotors. Table 1 states key technical data as found in [13].

Table 1: Technical key figures of Dragon 50.

Characteristic	Dragon 50	Unit
Engine	Jakadofsky Pro-X	
Engine Power	10.6	kW
Width	565	mm
Length	2267	mm
Height	970	mm
Rotor Diameter	2886	mm
Number of Blades	4	
Rotor RPM	950	1/min
Rotor Cant Angle	10.5	°
Max Useful Load	50	kg
Max Take-Off Weight (MTOW)	86	kg
Vmax (at cruise)[a]	15	m/s

[a] maximum autopilot speed allowed by manufacturer

To perform flight mechanical studies, the helicopter has been equipped with a measurement system based on a National Instruments cRIO device [13].

In this study, the measurements of interest are rotor shaft torque and hub moments. These are measured using a rotor telemetry that has been developed by the institute. The rotor telemetry serves a sample rate of 12.5 Hz.

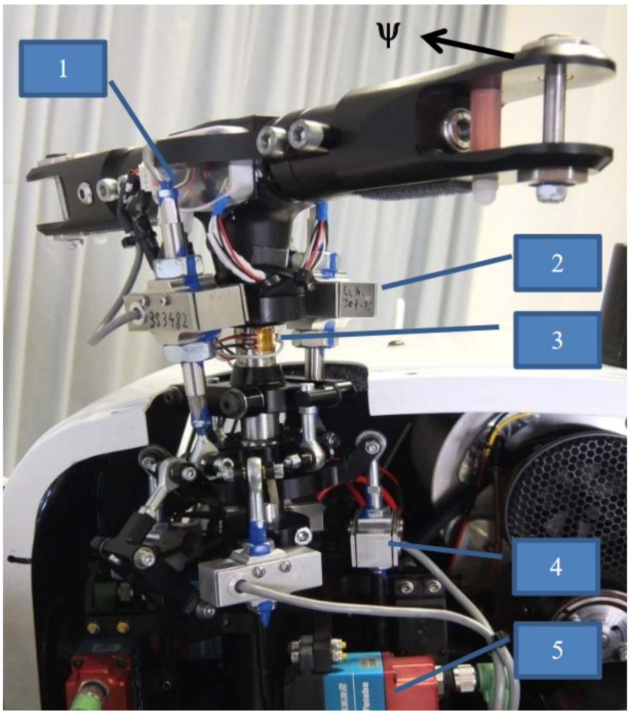

Figure 3: Instrumentation of the starboard rotor [13].

Figure 3 shows the rotor head with the aforementioned rotor telemetry. Part 1 resembles instrument transducers and a 2.4 GHz transceiver that transmits the measured excitations of strain gauges at the rotor shaft (Part 3) as well as control forces in the rotating system (Part 2) to the cRIO device. Not depicted in Figure 3 are strain gauges at the blade root which are used for measuring the flapping moment. The system is also capable of measuring pitch link forces. These are produced by the actuator (part 5) through steering rods (part 4) on the swashplate. In the rotating system, the steering forces are applied to the pitch link via force gauges (part 1).

5. Flight Tests

A trim curve for hover at different thrust settings has been gained by varying the fuel mass. By measuring rotor mast torsional strain on both rotors, we can calculate rotor power C_T (Figure 4). The test points obtained from the flight experiment are given in the appendix.

Rotor power is normalized as $C_P = \frac{P}{\rho A (\Omega R)^3}$

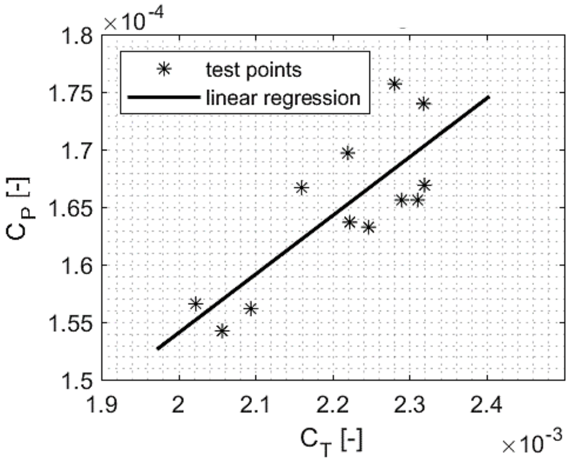

Figure 4: Flight test result for normalized rotor power in hover.

6. Numeric Simulation Setup

The flight mechanical model, incorporating respective inflow models, rigid blade flapping dynamics, and multibody dynamics, has been implemented within the Versatile Aerodynamic Simulation Tool (VAST). VAST, a simulation tool presently being developed by DLR, incorporates analytic and nonlinear descriptions of helicopter theory. It offers capabilities for flight performance studies, trim calculations, and transient calculations.

Throughout this study, we have integrated the CMTSVT model and the inflow modification proposed by Padthe et al. into the VAST inflow calculation subroutine. The rotor blades' inertial tensors, which were measured in reference [14], have been simplified in this paper to diagonal tensors to avert potential torsion-to-flapping coupling.

SuperARTIS showcases a hingeless blade attachment, which we model as a virtual flapping hinge. The stiffness of this hinge was obtained from internal documentation.

Table 2: Implemented rotor parameters.

Characteristic	Value	Uni t
Blades	2	
Profile	NASA RC(4)-10	
Flapping joint offset	0.25	m
Blade Root Cutout	0.25	m
Flapping-Torsion coupling Δ_3	0	deg
Blade Twist θ_{tw}	0	deg
Aspect Ratio Λ	16.03	
Surface density σ	0.0397	
Blade mass	0.715	Kg
Rotor cant angle	$\pm$10.5	deg
Blade tip velocity	143.56	m/s
Lift curve slope a	5.73	
Blade Inertial Tensor I_B	$diag([0.0005, 0.3535, 0.3469]$	

Padthe et al. chose $k^{ij} \neq k^{ji}$ as this is sensible for coaxial rotors. For the Flettner configuration, we choose a symmetric interaction, which leads to $k^{ij} = k^{ji}$ because rotors have the same height unlike the coaxial rotor configuration. The value of k^{ij} is extracted from the vortex model of CMTSVT as $k^{ij} = 0.92$. From earlier flight tests which studied the fast-forward flight regime, we estimated that the interaction effects phase out between 2.5 m/s and 15 m/s and set v_{cutoff} and v_{reduce} accordingly. A plausible reason for this could be the lateral displacement of the rotor downwashes in the Flettner configuration. Consequently, the interaction is decreased more rapidly in forward flight.

To compare the effects of the described inflow models on the flight mechanical simulation, we set up a simulation of hover trim varying collective pitch.

For the trim calculation, cyclic inputs were fixed to zero and collective was trimmed with the goal of setting vertical forces to zero. The time step was set to 0.87 ms equivalent to 5° blade angle change per time step. The fuselage is freezed in space.

7. Results and Discussion

Figure 5 depicts the trim results from flight test compared to the predictions from different inflow models. Using Pitt-Peters inflow model, the rotor thrust is significantly underestimated, while CMTSVT and the model by Padthe lead to a good match of the power prediction with flight test.

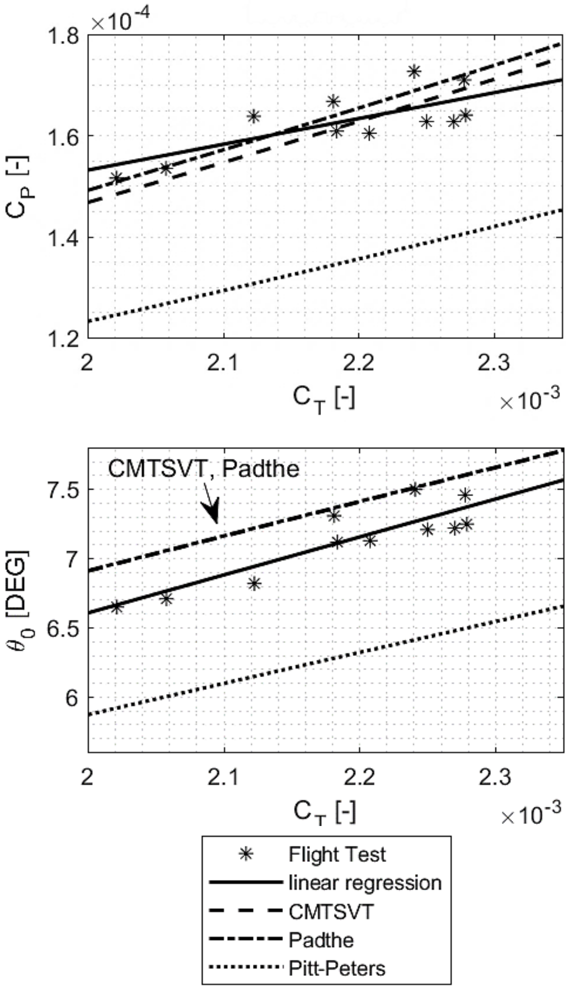

Figure 5: Hover Trim Results: Comparison of Rotor Power and collective command angle.

The error in collective control angle prediction using Pitt-Peters inflow is around 0.7 °. The CMTSVT and Padthe model improve this to an error of 0.3 °

Figure 6 depicts the distribution of induced inflow over the rotor disc in hover. While Pitt-Peters and Padthe inflow model show a uniform distribution, CMTSVT shows a strong lateral gradient. This gradient stems from the overlapping rotor configuration of the Dragon 50.

The inflow distribution of CMTSVT also shows a gradient in longitudinal direction.

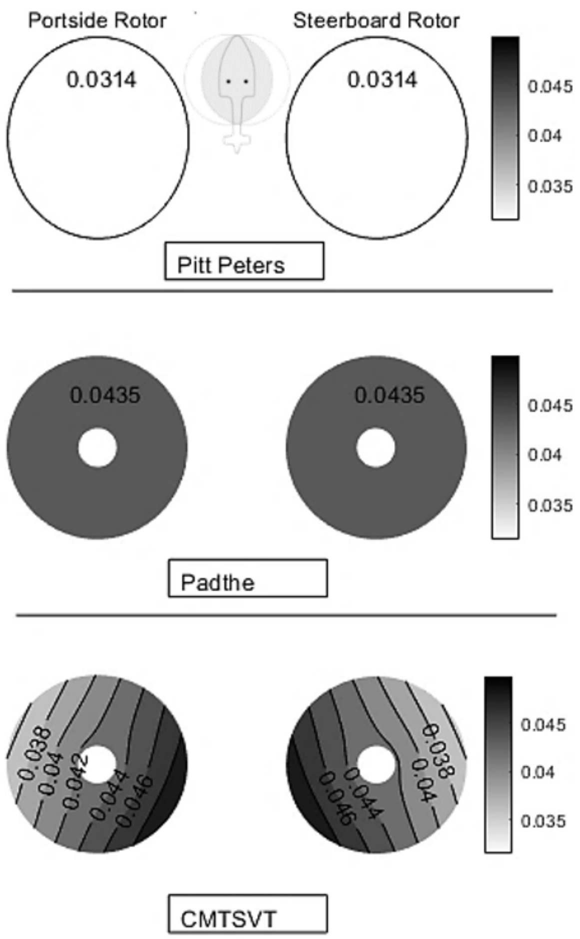

Figure 6: Induced velocity in hover, normalized in ΩR.
$C_T=2.0\cdot10^{-3}$.

The non-uniform inflow distribution predicted by the CMTSVT model leads to strong flapping moments, which in turn result in moments in roll and pitch. Due to the design of the Dragon 50 with its dual rotor, hingeless rotor head, these moments turn out relatively strong. Additional validation studies should be performed for these moments.

8. CONCLUSIONS

The comparison of the simulation results with flight test data lead to the following conclusions:

1. The rotor power prediction for intermeshing rotor configurations in hover need to include an inflow model that accounts for interference effects. CMTSVT model shows good matching with flight test data, making it a valuable tool for early design stages involving for example configuration studies.
2. A relatively simple coupling of separate inflow models that we observed in [11] leads to similar results in power predictions. In this case, the model parameter needs to be tuned using a reference inflow model or flight test results.
3. Intermeshing rotor configurations lead to strong hub loads due to interference effects. Uniform interference inflow is not adequate for simulating these loads. Additional validation studies should be performed to asses if these match the real moments.

Future work will involve modification of the flight test instrumentation to measure hub moments of first order. This will allow for the validation of predicted hub moments.

Author contact:

Tobias Ehlert: tobias.ehlert@dlr.de

Andreas Voigt: andreas.voigt@dlr.de

Feyyaz Guner: feyyaz.guener@dlr.de

9. APPENDIX

Table 4 shows the trim values from flight experiments that are used for evaluating the inflow models. They were gained by averaging the state variables over stationary hover states, outside ground effect. The data was averaged over 2 s to 6 s.

By varying the fuel mass, we achieved different rotor thrust in stationary hover. Thrust was then calculated analytically from the hover condition while the rotor power was measured using strain gauges on the rotor masts.

Table 4: Flight Test data points for hover analysis.

Mass	Power	Control Input			
		θ_c	θ_s	θ_0	Yaw
[kg]	[kW]	[DEG]	[DEG]	[DEG]	[DEG]
65.89	7.30	0.40	-0.13	6.62	0.69
67.01	7.19	-0.15	-0.02	6.65	0.00
68.11	7.28	-0.26	-0.04	6.71	-0.26
70.37	7.77	-0.29	-0.53	6.82	0.09
72.32	7.91	0.68	-0.14	7.31	-0.22
72.40	7.63	0.65	-0.21	7.12	-0.33
73.20	7.61	0.98	-1.16	7.13	-0.18
74.30	8.19	-0.34	-0.54	7.50	-1.87
74.6	7.72	1.23	-0.23	7.21	0.50
75.27	7.72	1.05	-0.04	7.22	0.17
75.52	8.81	0.80	-0.16	7.46	-0.27
75.56	7.78	0.74	-0.14	7.25	-0.23

10. REFERENCES

[1] F. Guner and J. V. R. Prasad, "Combined Momentum Theory and Simple Vortex Theory," *Journal of the American Helicopter Society, Vol. 67 (2),* 2022.

[2] F. Guner, "A Study to Examine Effects of the Inflow Interference on Induced Power," in *47th European Rotorcraft Forum Proceedings*, Virtual, 2021.

[3] D. Usov, W. Appleton, A. Filippone and N. Bojdo, "Low-Order Aerodynamic Model for Interference in Multirotor Systems," *Journal of Aircraft, Vol. 59 (6),* 2022.

[4] H. Glauert, “A general Theory of the Autogyro,” H. M. Stationery Office, 1926.

[5] H. Glauert, "The Theory of the Autogyro," *The Aeronautical Journal, Vol. 31 (198),* pp. 483-508, 1927.

[6] H. C. J. Curtiss, "Stability and Control Theory for Hingeless Rotors," in *Annual Forum of the American Helicopter Society*, Washington D.C., 1971.

[7] R. Ormiston and D. A. Peters, "Hingeless Helicopter Rotor Response with Nonuniform Inflow and Elastic Blade Bending," in *AIAA Aerospace Science Meeting*, San Diego, 1972.

[8] D. A. Peters and N. HaQuang, "Dynamic Inflow for Practical Applications: Technical Note," *Journal of the American Helicopter Society, Vol. 33 (4),* pp. 64-68, 1988.

[9] M. J. Bhagwat, "Transient Dynamics of Helicopter Rotor Wakes using a Time-Accurate Free-Vortex-Method. Disertation.," Maryland: University of Maryland, 2001.

[10] J. Hofmann and M. Röhrig-Zöllner, "Coupling Rotor Dynamics with a Parallel Airflow Simulation," in *ISC High Performance*, Frankfurt am Main, 2016.

[11] A. K. Padthe, E. D. Glover, M. J. S. Lopez, T. Berger, E. L. Tobias and O. Juhasz, "Design, Modeling, and Flight Dynamics Analysis of Generic Lift-Offset Coaxial Rotor Configurations," *Vertical Flight Society 79th Forum Proceedings,* vol. 78, 2022.

[12] F. Guner, "Evaluation of a Combined Momentum Theory and Simple Vortex Theory," in *Vertical Flight Society*

Aeromechanics for Advanced Vertical Flight Technical Meeting, San Jose, 2022.

[13] A. E. Voigt, J. Dauer, A. Krenik and J. S. Dittrich, "Detection of Forward Flight Limitations of Unmanned Helicopters," in *AHS 72nd Annual Forum*, West Palm Beach, Fl, 2016.

[14] F. Guner and J. V. R. Prasad, "Combined Momentum Theory and Simple Vortex Theory Inflow Model for Multirotor Configurations," *Journal of the American Helicopter Society,* 2022.

[15] F. Knaak, Entwicklung eines Verfahrens zur Bestimmung der aerodynamischen Kräfte aus der Rotorblattbewegung, Aachen: RWTH Aachen, 2017.

[16] W. Johnson, Helicopter Theory. Revised Edition, New York: Dover Publications, 1995.